Supporting Information

High Unsaturated Room-Temperature Magnetoresistance in Phase-Engineered $Mo_xW_{1-x}Te_{2+\delta}$ Ultrathin Films

Roshan Jesus Mathew,[a,b,c] Christy Roshini Paul Inbaraj,[a,b,d] Raman Sankar,[e,f] Shemsia Mohammed Hudie,[a,b,g] Revannath Dnyandeo Nikam,[h] Chi-Ang Tseng,[g] Chih-Hao Lee,[a] and Yit-Tsong Chen[*c,g]*

[a]Department of Engineering and System Science, National Tsing-Hua University, Hsinchu, Taiwan

[b]Nano-Science and Technology Program, Taiwan International Graduate Program, Academia Sinica, Taipei, Taiwan

[c]Institute of Atomic and Molecular Sciences, Academia Sinica, Taipei, Taiwan

[d]Department of Physics, National Taiwan University, Taipei, Taiwan

[e]Center for Condensed Matter Sciences, National Taiwan University, Taipei, Taiwan

[f]Institute of Physics, Academia Sinica, Taipei, Taiwan

[g]Department of Chemistry, National Taiwan University, Taipei, Taiwan

[h]Center for Emerging Electric Devices and Systems (CEEDS), Gwangju Institute of Sciences and Technology, Gwangju, South Korea

S1. The growth of $Mo_xW_{1-x}Te_2$/ *h*-BN in CVD reactions

In the CVD synthesis of $Mo_xW_{1-x}Te_2$ thin films, we adjusted the stoichiometric (molar) ratio between MoO_3 and a mixture of WO_3, WCl_6, and Te (of 1:1:1 weight ratio) as the chemical sources of Mo and W. The chemical precursors were mixed in a ceramic boat and placed downstream (Zone C) in the quartz tube of a furnace system (as illustrated in **Figure 1b** of the main text). Prior to the synthesis of $Mo_xW_{1-x}Te_2$ films, a ~11 nm thick *h*-BN film was grown on a Si wafer (denoted by *h*-BN/SiO_2/Si) of 1.8 ×1.8 cm^2 in size. The temporal temperature profiles for the growth of *h*-BN films in CVD reaction are given in **Figure S1a.** The optical image and AFM surface topography of the as-grown *h*-BN films are presented in **Figure S1b–d**.

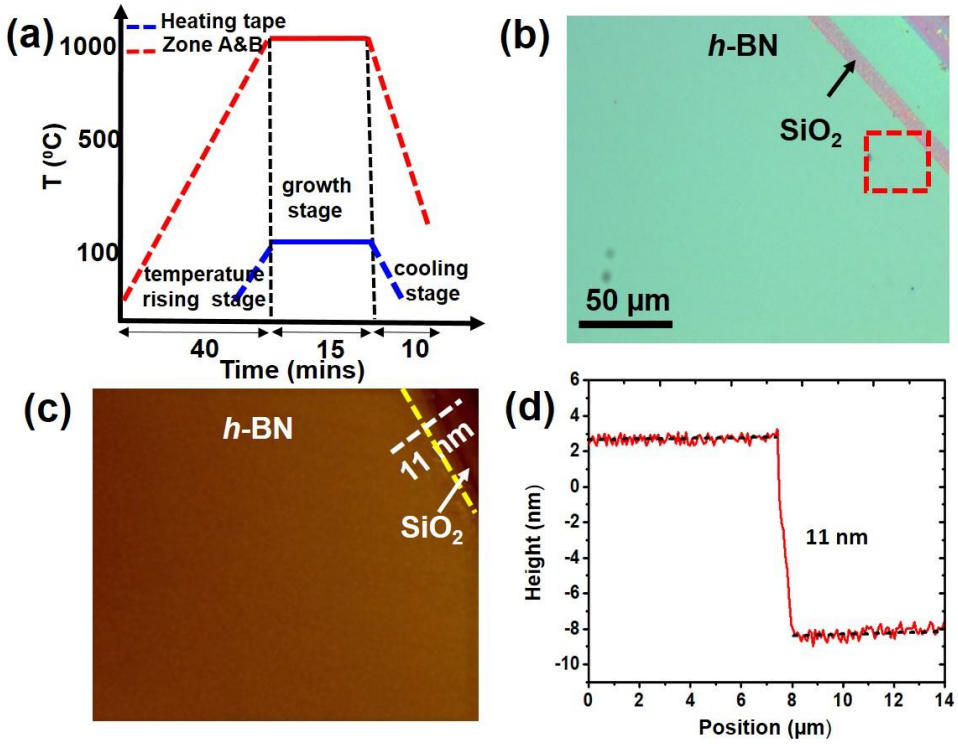

Figure S1. (a) The temporal temperature profiles are presented for the synthesis of *h*-BN thin films on a Si wafer (1.8 ×1.8 cm^2) in CVD reaction, including the early preparation, crystal growth, and cooling stages. (b) The optical microscopy image of a *h*-BN/SiO_2/Si substrate. (c–d) The surface topograph of the as-grown *h*-BN film on the SiO_2/Si surface (taken from the area

marked by the red dotted box in (b)) scanned by AFM gives the thickness of the *h*-BN film to be ~11 nm.

As illustrated in **Figure 1b** of the main text, this *h*-BN/SiO_2/Si substrate, to be used as a growth substrate for $Mo_xW_{1-x}Te_2$ films, was located in Zone C and placed on (with the side of *h*-BN facing down) a ceramic boat filled containing the chemical precursors with an adjustable stoichiometric (molar) ratio between MoO_3 and a mixture of WO_3, WCl_6, and Te (with the weight ratio of 1:1:1). The CVD reaction was facilitated by Te, in which the high melting point of metal oxide (MO_x, M = Mo or W) precursors could be reduced thermodynamically via the eutectic point of MO_x and Te at ~450 °C.[S1,S2]

In the upstream region of Zone B, we put 200 mg of Te powder on a quartz plate above a ceramic boat as the Te source. While the growth time was kept 7–15 min to produce ~2–13 nm thick $Mo_xW_{1-x}Te_2$ thin films, a shorter growth time (<7 min) could yield only $Mo_xW_{1-x}Te_2$ nanoflakes. The synthesis of $Mo_xW_{1-x}Te_2$ films in the CVD reaction includes three steps: (i) the formation of metal oxychloride, (ii) the decomposition of metal oxychloride and the reduction of metal oxides, and (iii) the tellurization. During the growth of a $Mo_xW_{1-x}Te_2$ film, the temperatures at Zone B and Zone C were kept 550 °C and 820 °C, respectively, as the temperature profile shown in **Figure S2a**.

In Zone C, when the temperature was increased to 200 °C during the reaction, Te could react with WCl_6 to form $Te_4(WCl_6)_2$.[S3] However, $Te_4(WCl_6)_2$ is unstable above 280 °C and could decompose back to Te and WCl_6.[S3,S4] Therefore, when the reaction temperature was raised to 280 °C, the molten WCl_6 (melting point of 275 °C) could react with the metal oxides (MO_x, M = Mo and W) to form a metal oxychloride (as listed in Equation (1)), [S5,S6] which was

subsequently decomposed to metal oxides and chlorine gas (Equation (2)) as the reaction temperature increased to 350 °C.

$$12MoO_3 + 6WO_3 + 6WCl_6 \rightarrow 12MoWOCl_3 + 21\ O_2\ (g) \quad (1) \quad \text{at } 280\ °C$$

$$6MoWOCl_3 \rightarrow MoO_3 + WO_3 + 9Cl_2\ (g) + 5Mo + 5W \quad (2) \quad \text{at } 350\ °C$$

When the reaction temperature reached 450 °C in Zone C, the high melting point of MO_x could be reduced thermodynamically via the eutectic point (~450 °C) of MO_x and Te and the reduction of MO_x could be facilitated by reacting with WCl_6. Meanwhile, the Te vaporized at Zone B and flowed to Zone C. To facilitate the reduction reaction, H_2 was introduced at 760 °C to initiate the formations of H_2Te (Equation (3)), which then reacted with metals to form M–Te (M = Mo and W) at >760 °C (Equation (4)).[S7] The reactive species of M–Te in turn drove the nucleation growth of $Mo_xW_{1-x}Te_2$ film at 820 °C (Equation (5)). At even higher growth temperature (>820 °C), some unreduced oxides (MoO_3 and/or WO_3,) would be left after the reaction; [S8] however, the oxides could be removed efficiently by post-annealing. [S9]

$$2Te + H_2 \rightarrow H_2Te \quad (3) \quad \text{at } 760\ °C$$

$$M + H_2Te \rightarrow M–Te + H_2\ \ (M = Mo_x \text{ or } W_{1-x}) \quad (4) \quad \text{at } 760\ °C < T < 820\ °C$$

$$Mo_x–Te + W_{1-x}–Te \rightarrow Mo_xW_{1-x}Te_2 \quad (5) \quad \text{at } 820\ °C$$

Introducing H_2 to the reaction plays a crucial role in facilitating the metal tellurization and enhancing the reduction of metal oxides. From the synthesis, we found that uniform films of the desired stoichiometry could be produced by introducing H_2 at 760 °C, whereas Mo-rich films would be formed by introducing H_2 at 650–760 °C. These results might be due to the fact that MoO_3 could be reduced to Mo at lower temperature than WO_3, where Mo has higher reactivity

than W to react with Te. It is noted that H_2 was introduced only after the vaporization of Te (~450 °C), assuring that H_2Te reacted with metals (Mo and W).

In the synthesis of $Mo_xW_{1-x}Te_2$ at high reaction temperature (>760 °C, Equations (4) & (5)), the Mo−Te bond is difficult to form, because the Te atoms of $MoTe_2$ could substantially sublimate. However, the formation of Mo−Te (Equations (4)) is critical for the subsequent alloy formation (Equation (5)); therefore, to maintain a high supply rate of Te is essential for the formation of $Mo_xW_{1-x}Te_2$ with a desired stoichiometric ratio.[S1,S9] Moreover, the time- and temperature-dependent tellurization kinetics are vital for yielding semimetallic $Mo_xW_{1-x}Te_2$ thin films, where the fast vaporization of Te to keep excessive Te vapor and the quick cooling of growth products after the CVD reaction are critical for successfully synthesizing these alloy films. In the processes of Synthesis Route I and Synthesis Route II, both reactions involved the same synthetic protocols except that the cooling rate of 90 °C/min was set for the former and 15 °C/min was applied for the latter. The rapid cooling procedure of the synthesized films by Synthesis Route I was performed at an Ar flow of 600 sccm and quickly drawing the growth substrate out of the hot zone assisted by a magnet. The synthesis methods (both Routes I and II) are highly reproducible in terms of the composition ratios and crystal phases of the as-synthesized $Mo_xW_{1-x}Te_2$ films. In **Figure S2**, the surface image and film thickness of the as-synthesized T_d-$Mo_{0.27}W_{0.71}Te_{2.02}$ thin films (Synthesis Route I) on the SiO_2/Si and *h*-BN/SiO_2/Si substrates, respectively, were investigated. Similar investigations of the as-synthesized *2H*- & T_d-$Mo_{0.22}W_{0.89}Te_{1.89}$ thin films (Synthesis Route II) on the SiO_2/Si and *h*-BN/SiO_2/Si substrates, respectively, are given in **Figure S3**.

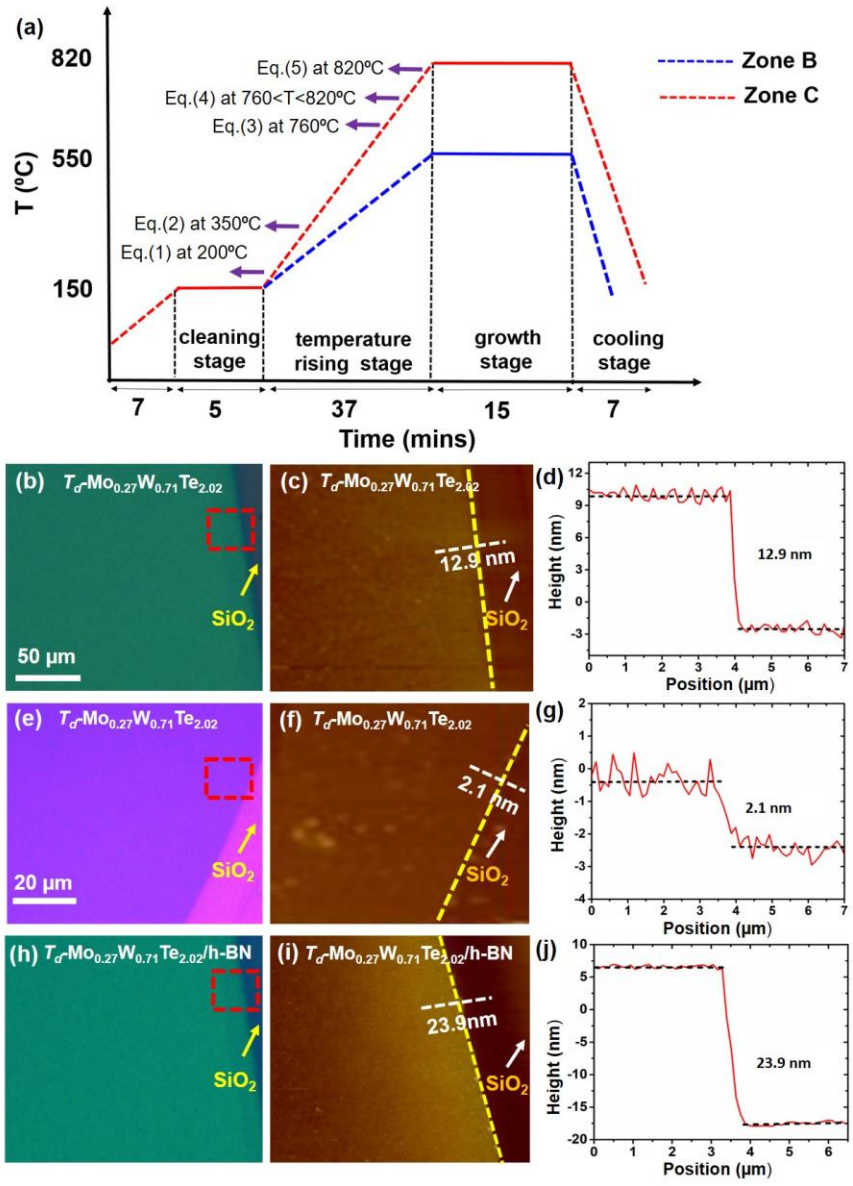

Figure S2. (a) The temporal temperature profiles are presented for the synthesis of T_d-$Mo_{0.27}W_{0.71}Te_{2.02}$ thin films (Synthesis Route I) in CVD reactions. (b–g) The optical microscopy and AFM images of the as-synthesized T_d-$Mo_{0.27}W_{0.71}Te_{2.02}$ films on a SiO_2/Si substrate reveal the film thicknesses of (b–d) ~12.9 nm under 15 min CVD growth and (e–g) ~2.1 nm under 7 min growth. (h–j) Comparatively, a T_d-$Mo_{0.27}W_{0.71}Te_{2.02}$ film grown on a *h*-BN/SiO_2/Si substrate gives a total height (including the T_d-$Mo_{0.27}W_{0.71}Te_{2.02}$ and *h*-BN films) of ~23.9 nm under 15 min CVD growth.

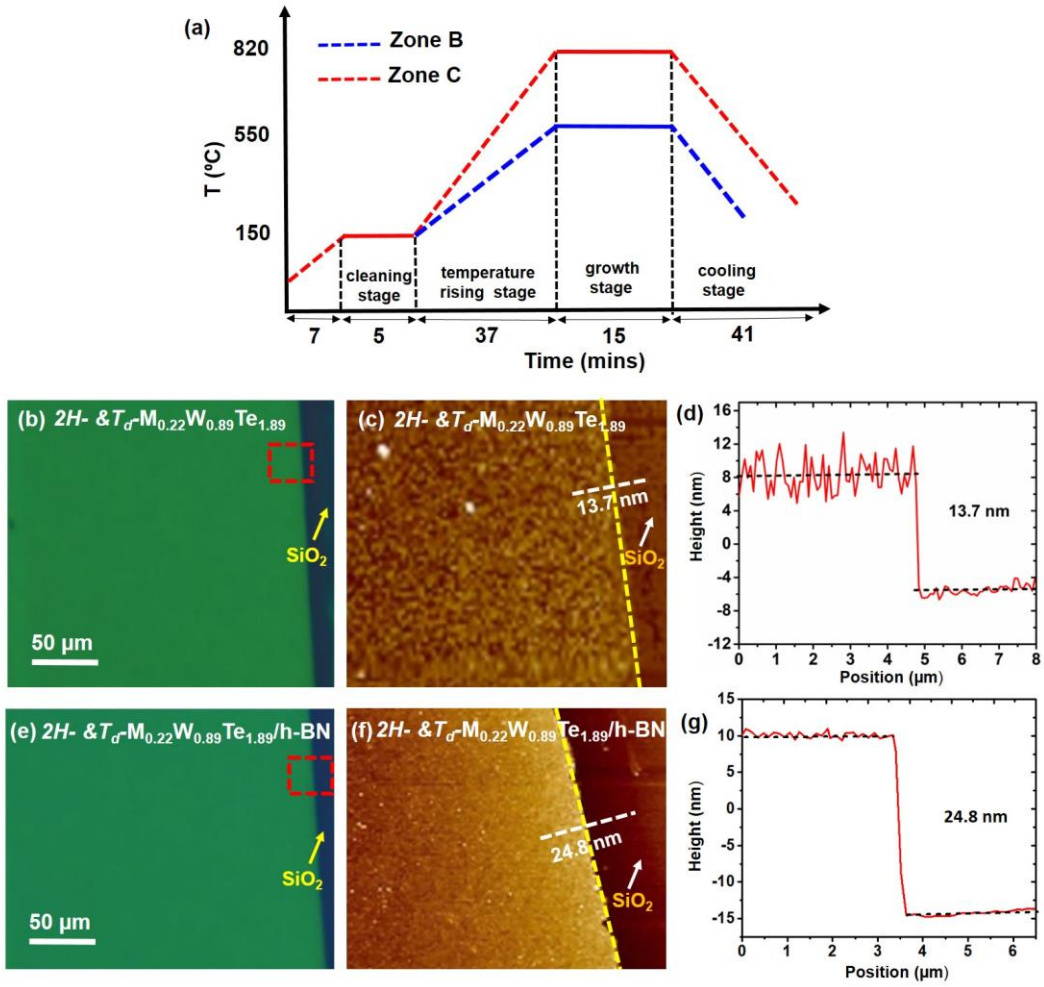

Figure S3. (a) The temporal temperature profiles are presented for the synthesis of *2H- & T_d*-$Mo_{0.22}W_{0.89}Te_{1.89}$ thin films (Synthesis Route II) in CVD reactions. The optical microscopy and AFM images of the as-synthesized *2H- & T_d*-$Mo_{0.22}W_{0.89}Te_{1.89}$ films on (b–d) a SiO_2/Si substrate with the grown film of ~13.7 nm in thickness under 15 min CVD growth and (e–g) a *h*-BN/SiO_2/Si substrate with a total height (including the *2H- & T_d*-$Mo_{0.22}W_{0.89}Te_{1.89}$ and *h*-BN films) of ~24.8 nm under 15 min growth.

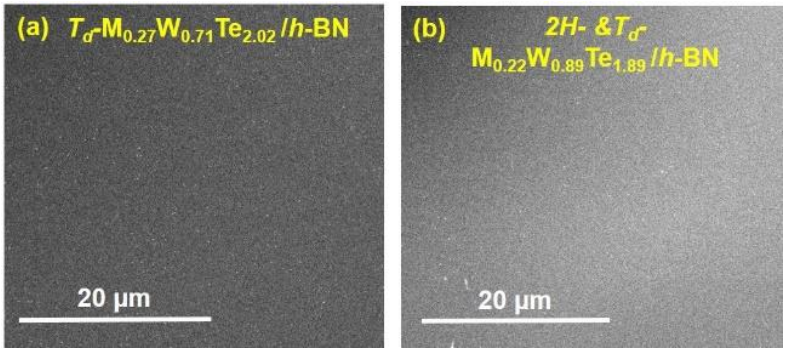

Figure S4. The SEM images of (a) T_d-$Mo_{0.27}W_{0.71}Te_{2.02}$ (Synthesis Route I) and (b) *2H- & T_d*-$Mo_{0.22}W_{0.89}Te_{1.89}$ (Synthesis Route II) thin films were scanned over an area of 40×40 μm^2.

S2. CVT growth of T_d-$Mo_{0.29}W_{0.68}Te_{2.03}$ bulk crystal

The bulky T_d-$Mo_{0.29}W_{0.68}Te_{2.03}$ single crystal was synthesized via a CVT method using iodine as the transport agent. The Mo and W powders (99.99% in purity), Te pellets (99.999% in purity), and iodine (99.999% in purity, 5.8 mg/cm^3) were introduced into a quartz tube, then evacuated, heated to 1150 ^{o}C, and held at this temperature for 1.5 weeks at a temperature gradient of ~100 ^{o}C/day. Subsequently, the quartz tube was cooled to 1050 ^{o}C at a rate of 10 ^{o}C/h, followed by another cooling process at 2 ^{o}C/h to 800 ^{o}C, then held at 800 ^{o}C for 2 days, and finally quenched in air.

S3. Spectral analysis by X-ray photoelectron spectroscopy (XPS)

The XPS spectra were calibrated against the binding energy of adventitious hydrocarbon C 1s signal at 284.60 eV prior to spectral processing, which was also used as the reference energy to correct the background charging effect. The spectral background subtraction was made with the Shirley-Sherwood method. The quantitative elemental composition was calculated by integrating the highest intensity peak of each element and considering their respective atomic sensitive factors.

The XPS spectra of the CVD-grown *h*-BN on a Si wafer (referred to as *h*-BN/SiO_2/Si, to be used as a substrate for the subsequent $Mo_xW_{1-x}Te_2$ growth) are shown in **Figure S5.** The O–B–N peak in the B 1s spectrum (**Figure S5a**) confirms that the location of O worked as the nucleation site of B, which subsequently connected N to form a uniform *h*-BN film.[S10] The B−O peak also suggests the presence of boron-terminated edges bonding to the SiO_2/Si growth substrate. In contrast, the absence of the N−O peak in the N 1s spectrum (**Figure S5b**) implies that N bound with B only, but not with the O of SiO_2/Si[S10] The O 1s spectrum (**Figure S5c**) of the *h*-BN film further confirms the bonding between B and O, in which the peak at ~530 eV is likely due to the physically adsorbed O_2.

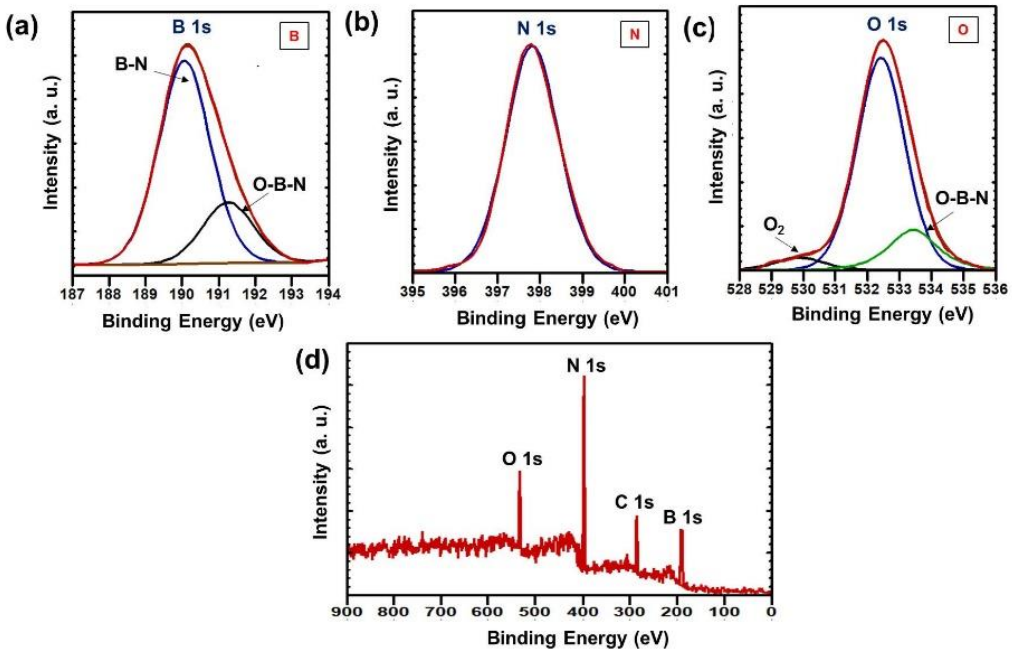

Figure S5. The XPS spectra of the *h*-BN film grown on a Si wafer show the spectral features of (a) boron (B 1s), (b) nitrogen (N 1s), and (c) oxygen (O 1s). (d) A wide range XPS spectrum of the as-grown *h*-BN/SiO_2/Si is presented.

The residual oxides left on the as-synthesized $Mo_xW_{1-x}Te_2$ films could be successfully removed by annealing the $Mo_xW_{1-x}Te_2$ films with an Ar (1 atm) flow at 475 °C. Shown in **Figure S6** is the comparison of the XPS spectra of a T_d-$Mo_{0.27}W_{0.71}Te_{2.02}$ (Synthesis Route I) film, before and after annealing, where the residual oxides were removed efficiently by thermal annealing.

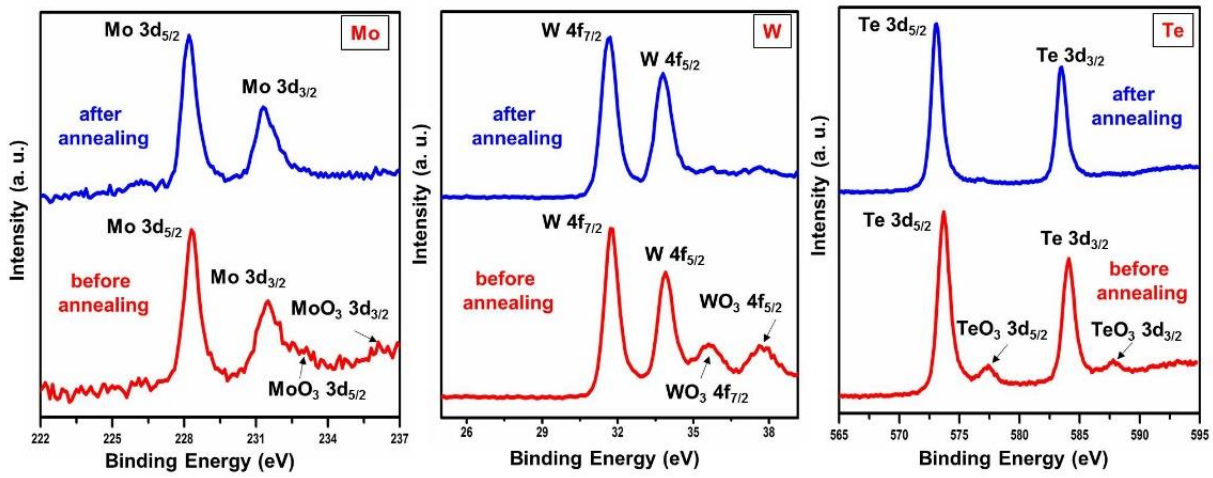

Figure S6. The residual oxides left on the CVD-grown $Mo_xW_{1-x}Te_2$ films could be removed efficiently by thermal annealing, which are evidenced by the sharp contrast, between the XPS spectra of the as-synthesized T_d-$Mo_{0.27}W_{0.71}Te_{2.02}$/h-BN (Synthesis Route I) thin film, before and after annealing.

The compositions of $Mo_xW_{1-x}Te_2$ play a crucial role in modulating the phases of this alloy system. In this study, we analyzed the spectral features in the observed XPS spectra to obtain the stoichiometric ratios of the CVD-grown $Mo_{0.27}W_{0.71}Te_{2.02}$ (Synthesis Route I, **Figure S7**) and $Mo_{0.22}W_{0.89}Te_{1.89}$ (Synthesis Route II, **Figure S8**) thin films and the CVT-grown $Mo_{0.29}W_{0.68}Te_{2.03}$ (bulk crystal, **Figure S8**). The quantitative elemental composition was calculated by integrating the intensity of the Mo $3d_{5/2,}$ W $4f_{7/2}$, and Te $3d_{5/2}$ peaks by taking their respective atomic sensitive factors into account. The atomic sensitivity factors used were 1.66 for Mo $3d_{5/2}$, 1.76 for W $4f_{7/2}$, and 5.71 for Te $3d_{5/2}$. With the composition ratios determined from our XPS analyses, we could attribute the samples obtained from both CVD-Synthesis Route I and CVT-grown bulk samples to the T_d phase according to the earlier studies of composition-dependent phase transitions; [S11,S12] likewise, the excessive W-containing, but

deficient Te, crystal obtained from CVD-Synthesis Route II was assigned to possess the co-existence of *2H* and T_d phases. A similar co-existence of *2H* and T_d phases in the Te-deficient alloy system of $WSe_{2(1-x)}Te_{2x}$ was also reported recently.[S13]

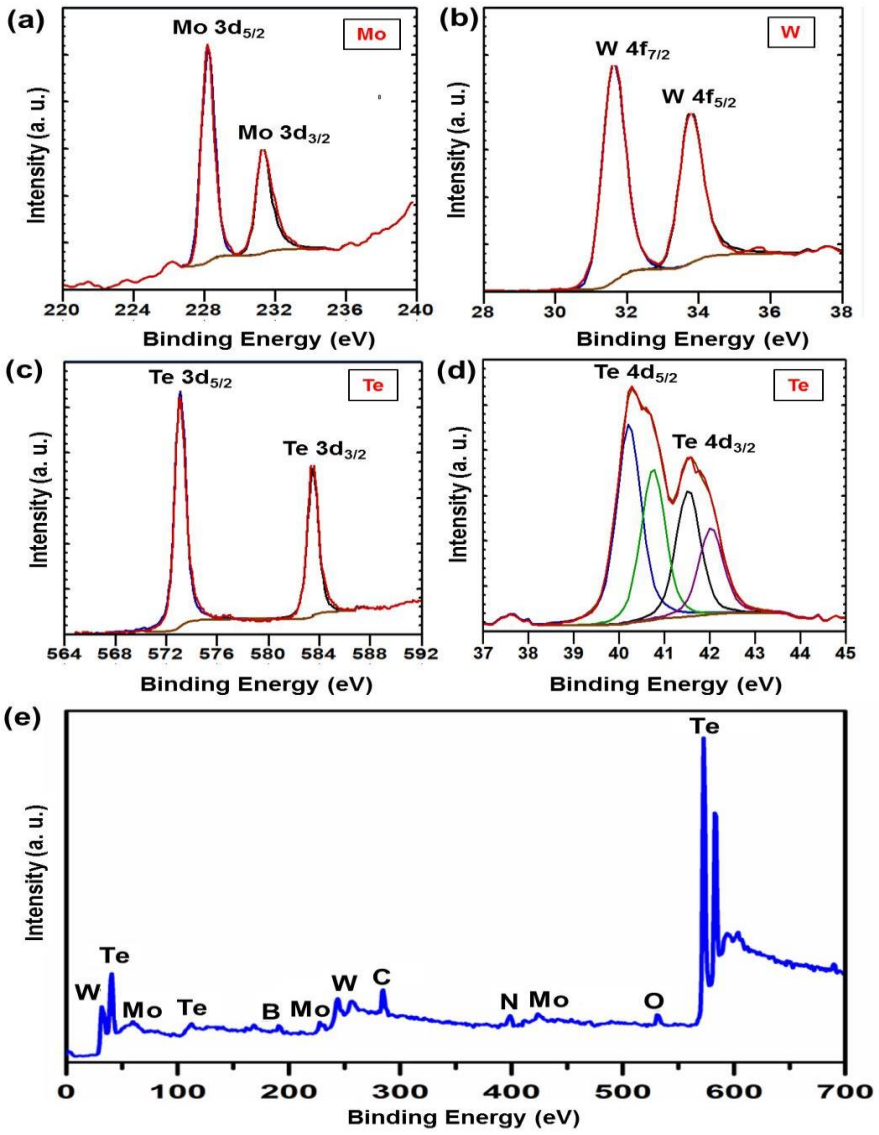

Figure S7. The XPS spectra of the T_d-$Mo_{0.27}W_{0.71}Te_{2.02}$ (Synthesis Route I) film after annealing at 475 °C show the doublets caused by the spin-orbit couplings of (a) $3d_{5/2}$ (227.8 eV) and $3d_{3/2}$ (231.0 eV) in Mo, (b) $4f_{7/2}$ (31.3 eV) and $4f_{5/2}$ (33.4 eV) in W, and (c) $3d_{5/2}$ (572.4 eV) and $3d_{3/2}$ (582.7 eV) in Te. (d) The doublets of $4d_{5/2}$ and $4d_{3/2}$ in Te further split into four peaks at 40.22 eV, 40.75 eV, 41.54 eV, and 42.04 eV, suggesting that the Mo/W layer is sandwiched by Te

atoms[S14] (e) A wide-range XPS spectrum of a T_d-$Mo_{0.27}W_{0.71}Te_{2.02}$ film on *h*-BN/SiO_2/Si covering all of the elemental constituents, showing that no other undesired elements are present in the synthesized thin films.

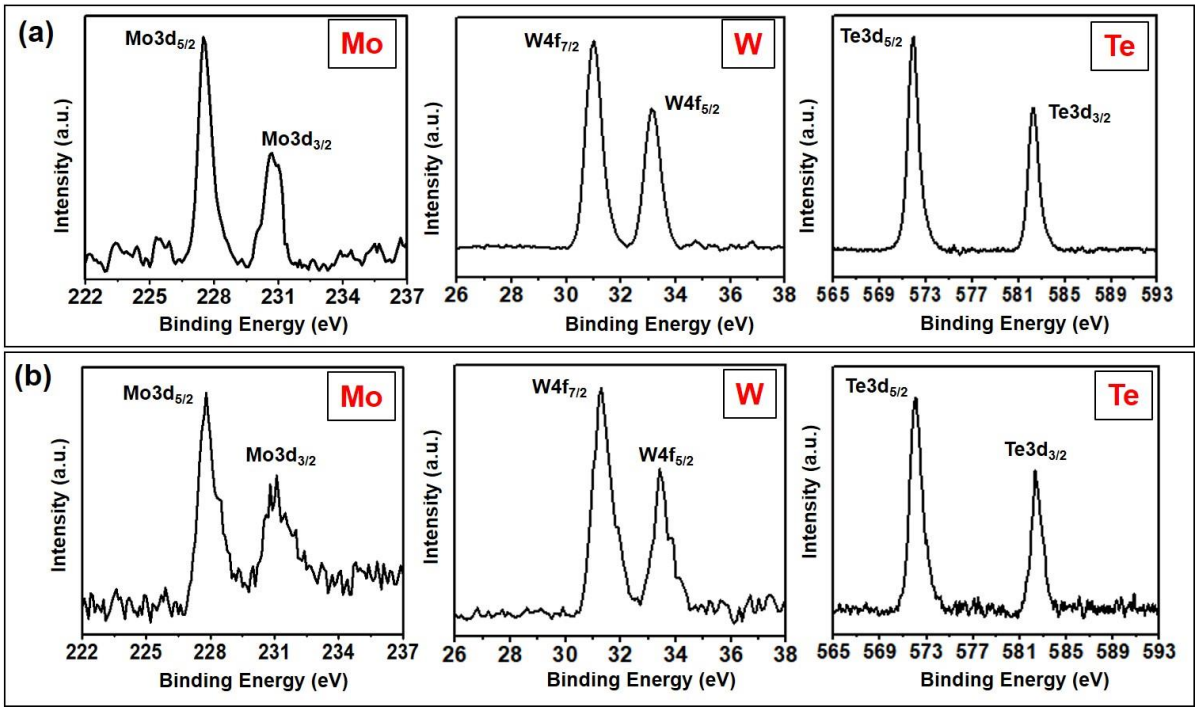

Figure S8. The doublets caused by the spin-orbit coupling in Mo, W, and Te, respectively, were observed in the XPS spectra of an annealed sample of (a) *2H*- & T_d-$Mo_{0.22}W_{0.89}Te_{1.89}$/*h*-BN (Synthesis Route II) with $3d_{5/2}$ (227.51 eV) and $3d_{3/2}$ (230.73 eV) in Mo, $4f_{7/2}$ (30.94 eV) and $4f_{5/2}$ (33.181 eV) in W, and $3d_{5/2}$ (571.83 eV) and $3d_{3/2}$ (582.48 eV) in Te. (b) The XPS spectra of an annealed sample of T_d-$Mo_{0.29}W_{0.68}Te_{2.03}$ (bulk crystal) show $3d_{5/2}$ (227.81 eV) and $3d_{3/2}$ (231.13 eV) in Mo, $4f_{7/2}$ (31.24 eV) and $4f_{5/2}$ (33.56 eV) in W, and $3d_{5/2}$ (572.20 eV) and $3d_{3/2}$ (582.61 eV) in Te.

S4. Structural characterizations by Raman spectroscopy

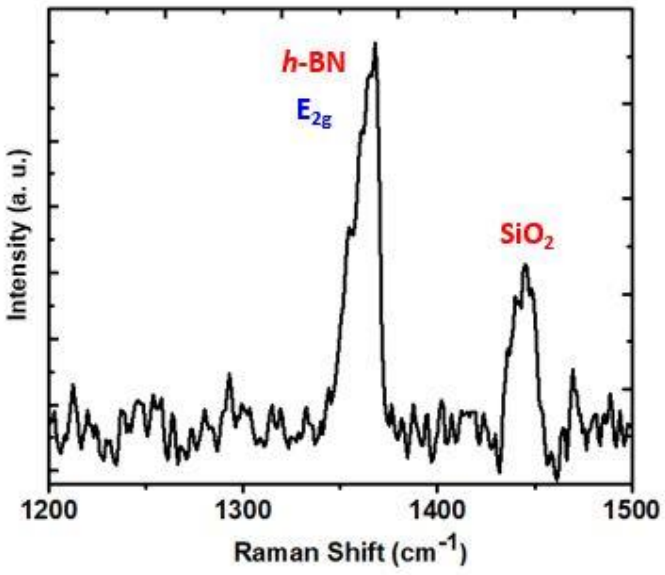

Figure S9. The E_{2g} band of a *h*-BN thin film synthesized on a SiO_2/Si substrate was observed in the Raman spectrum with the excitation wavelength of 785 nm.

In **Figure S10a**, the Raman spectra of T_d-$Mo_{0.27}W_{0.71}Te_{2.02}$ thin film (Synthesis Route I), *2H*- & T_d-$Mo_{0.22}W_{0.89}Te_{1.89}$ thin film (Synthesis Route II), and T_d-$Mo_{0.29}W_{0.68}Te_{2.03}$ bulk crystal are compared and analyzed**.**

The Raman measurements were carried out using a 532 nm laser of 1.07 mW power guided by a grating of 1800 g/mm through a 50× objective lens. The first-order Raman scattering of Si at 520 cm^{-1} was used as a calibration reference.

Alloy characteristics. In the observed Raman spectra of the as-synthesized T_d-$Mo_{0.27}W_{0.71}Te_{2.02}$ (Synthesis Route I) and *2H*- & T_d-$Mo_{0.22}W_{0.89}Te_{1.89}$ (Synthesis Route II) films, the peak splitting at ~129 cm^{-1} (A_1^5) is caused by both inversion symmetry breaking and random

metal-atom substitutions. This splitting of the ~129 cm^{-1} (A_1^5) peak agrees with the report of the $Mo_xW_{1-x}Te_2$ bulk crystal, [S11, S12] where a doublet with the separation of ~3 cm^{-1} was observed. In the Raman spectra of our synthesized T_d-$Mo_{0.27}W_{0.71}Te_{2.02}$ and *2H*- & T_d-$Mo_{0.22}W_{0.89}Te_{1.89}$ thin films, the broad A_1^5 band was deconvoluted into three peaks at 128.9, 131.9, and 134.9 cm^{-1} (in the inset of **Figure 1g** and **Figure S10b**). These splittings in the A_1^5 mode are attributed to both the phonon confinement to cause frequency shift and the linewidth broadening when the thickness of a layered material is reduced.[S15-S17] Another very weak peak at 178 cm^{-1} is attributed to the activated infrared mode due to the loss of lattice translation symmetry, resulting from the random positioning of dopant atoms in the alloy of $Mo_xW_{1-x}Te_2$. [S18]

Film thickness. The blue shifts of the entire Raman phonon modes, especially for the in-plane (A_1^3) and out-of-plane (A_1^5) low-frequency vibrations in the CVD-synthesized alloy films (both Synthesis Routes I & II) as compared with those of the bulk counterpart, also support the vibrational nature of an ultrathin crystal. As the thickness of a crystal reduces, these anomalous blue-shifts of Raman modes are caused by the stacking-induced dielectric screening of the long-range Coulomb forces.[S19] Moreover, the ultrathin $Mo_xW_{1-x}Te_2$ films possess the characteristics of softening the A_1^3 mode and stiffening the A_1^5 and A_1^7 modes; similar features were observed in few-layered WTe_2 films.[S20]

Phase identification. In **Figure S10a**, the two strong Raman signals at 162 and 212 cm^{-1} are attributed to the A_1^7 and A_1^9 phonon modes of the T_d phase, which appear in both T_d-$Mo_{0.27}W_{0.71}Te_{2.02}$ (middle blue trace) and *2H*- & T_d-$Mo_{0.22}W_{0.89}Te_{1.89}$ (upper green trace). Nevertheless, in the Raman spectrum of *2H*- & T_d-$Mo_{0.22}W_{0.89}Te_{1.89}$ (upper green trace), in addition to these two strong A_1^7 and A_1^9 signals, several medium and weak Raman signals show

up in the higher-frequency tails of these two A_1^7 and A_1^9 peaks. To analyze these medium and weak Raman signals of *2H*- & T_d-$Mo_{0.22}W_{0.89}Te_{1.89}$ (upper green trace), we have deconvoluted the Raman signals in the 145–250 cm^{-1} region as shown in **Figure S10c**. For clarity, we summarize the deconvoluted Raman signals of T_d-$Mo_{0.27}W_{0.71}Te_{2.02}$ (middle blue trace) and *2H*- & T_d-$Mo_{0.22}W_{0.89}Te_{1.89}$ (upper green trace) in the following table.

T_d-$Mo_{0.27}W_{0.71}Te_{2.02}$ (Route I) (peak position)	Raman Modes	*2H*- & T_d-$Mo_{0.22}W_{0.89}Te_{1.89}$ (Route II) (peak position)	Raman Modes
80/87	A_2^2	79/86	A_2^2
104/114	A_1^3	102/112	A_1^3
129	A_1^5	128	A_1^5
162	A_1^7	160	A_1^7
		173	A_{1g} *(2H)*
		200	E_{1g} *(2H)*
212	A_1^9	210	A_1^9
225	A_g^1	223	A_g^1
		234	E_{2g}^1 *(2H)*
271	A_1^{11}	269	A_1^{11}

In the Raman spectrum of *2H*- & T_d-$Mo_{0.22}W_{0.89}Te_{1.89}$ (upper green trace of **Figure S10a** and **c**), the A_{1g}, E_{1g}, and E_{2g}^1 modes of *2H*-$MoTe_2$ are responsible for the peaks at 173, 200, and 234 cm^{-1}.[S11, S21-S23] While the peak at 173 cm^{-1} is attributed to the in-plane metal-chalcogen vibration of *2H*-$MoTe_2$, the 234 cm^{-1} peak is assigned to the out-of-plane chalcogen vibration of *2H*-$MoTe_2$.[S23] Moreover, the peak at 200 cm^{-1} is reported due to a double-resonance Raman mode in few-layered *2H*-$MoTe_2$, resulting from the scattering of longitudinal and acoustic phonons from the M-point of the Brillouin zone.[S11, S21]

It is noted that the peak at ~225 cm^{-1} represents the A_g^1 mode of T_d-WTe_2, which has been

studied to co-exist with the A_1^9 phonon mode with a small frequency difference.[S24, S25].

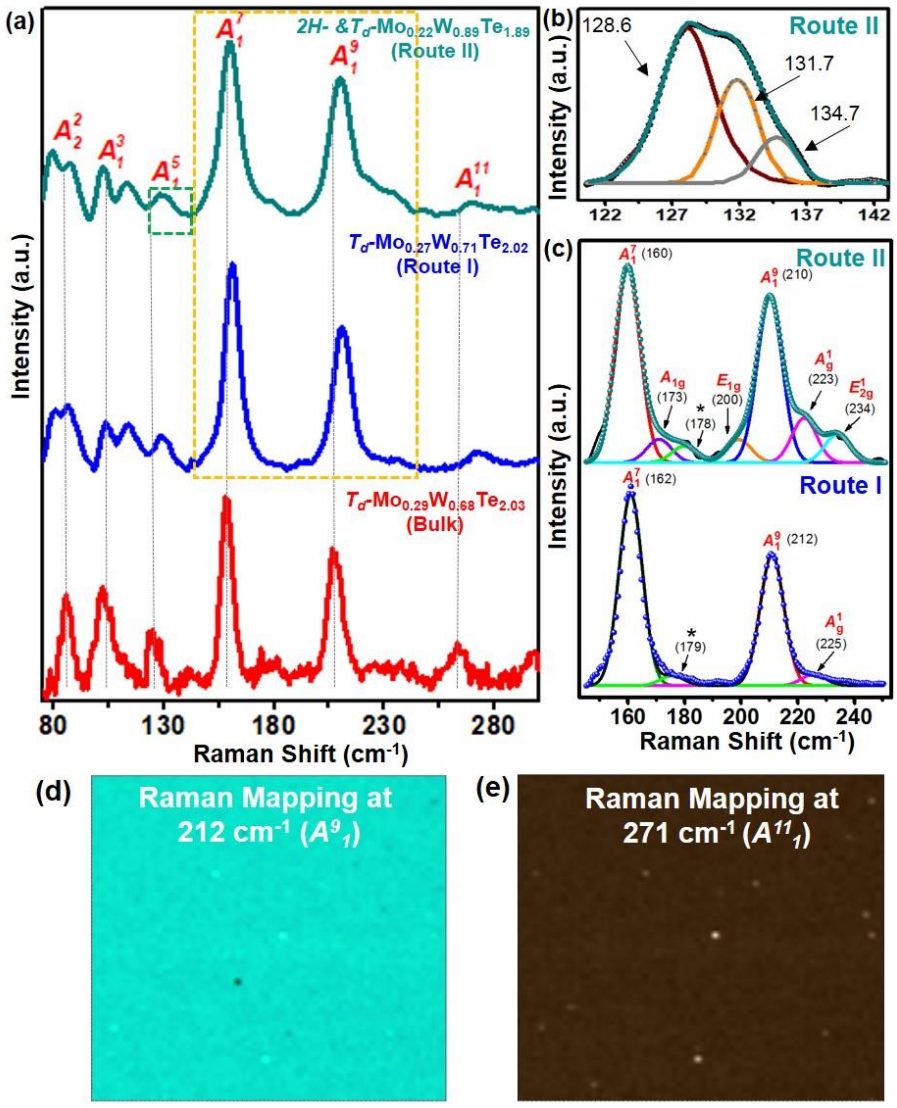

Figure S10. (a) A comparison of the Raman spectra of CVD-grown *2H*- & T_d-$Mo_{0.22}W_{0.89}Te_{1.89}$ (Synthesis Route II, top), T_d-$Mo_{0.27}W_{0.71}Te_{2.02}$ (Synthesis Route I, middle), and CVT-grown T_d-$Mo_{0.29}W_{0.68}Te_{2.03}$ (bulk crystal, bottom). The Raman spectra were excited with a 532 nm laser. (b) The deconvoluted Raman spectrum at 120–145 cm^{-1}, magnified from the green dotted box in (a) for Synthesis Route II sample, is presented in an expanded scale. (c) The deconvoluted Raman spectrum at 145–250 cm^{-1}, magnified from the orange dotted box in (a) for Synthesis Route I (blue curve) and II (green curve) samples, is presented in an expanded scale.

S5. Transmission electron microscopy (TEM) analysis

TEM sample preparation: 30 µL of polymethylmethacrylate (PMMA) solution was spin-coated onto a $Mo_xW_{1-x}Te_2$/*h*-BN-containing Si wafer, first at 1000 rpm for 10 sec, followed by 3000 rpm for 60 sec. After baking at 120 °C for 15 min, the PMMA-coated substrate was immersed into 0.5 M NaOH to etch the interfacial SiO_2 layer. The PMMA/$Mo_xW_{1-x}Te_2$/*h*-BN film, detached from the Si wafer, was bailed out with a coverslip and washed multiple times with deionized water. The PMMA/$Mo_xW_{1-x}Te_2$/*h*-BN film floating on the deionized water was then picked up carefully by a Lacey carbon-coated TEM grid and dried at 180 °C for 3 min. The PMMA coat was finally washed off with acetone and the HR-TEM images of $Mo_xW_{1-x}Te_2$/*h*-BN were taken in a TEM system.

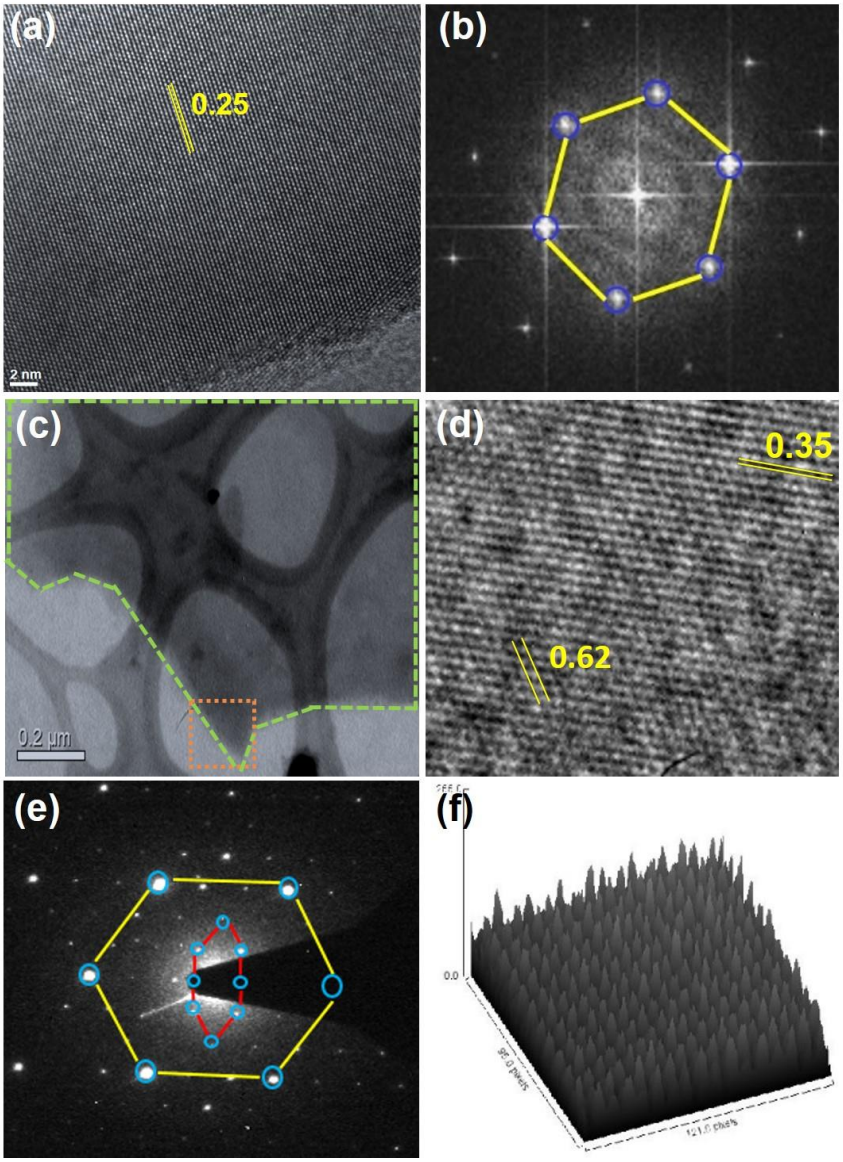

Figure S11. (a) HR-TEM image and (b) the corresponding FFT pattern of the synthesized *h*-BN thin film show a hexagonal geometry with the lattice spacing of 0.25 nm (c) The TEM image of a T_d-$Mo_{0.27}W_{0.71}Te_{2.02}$/*h*-BN thin film (demarcated by green dotted line), which was transferred on a Leicy carbon support for the TEM measurement, is presented. (d) HR-TEM image and (e) SAED pattern (taken from the orange dotted box in Panel (c)) of T_d-$Mo_{0.27}W_{0.71}Te_{2.02}$/*h*-BN. The SAED pattern reveals the high crystallinity in both orthorhombic T_d-$Mo_{0.27}W_{0.71}Te_{2.02}$ (demarcated by a red hexagon) and hexagonal *h*-BN (linked by a green hexagon). (f) A 3D surface profile of a T_d-$Mo_{0.27}W_{0.71}Te_{2.02}$/*h*-BN with the corresponding HR-TEM pattern shown in Panel (d).

S6. Electric transport measurements by physical property measurement system (PPMS)

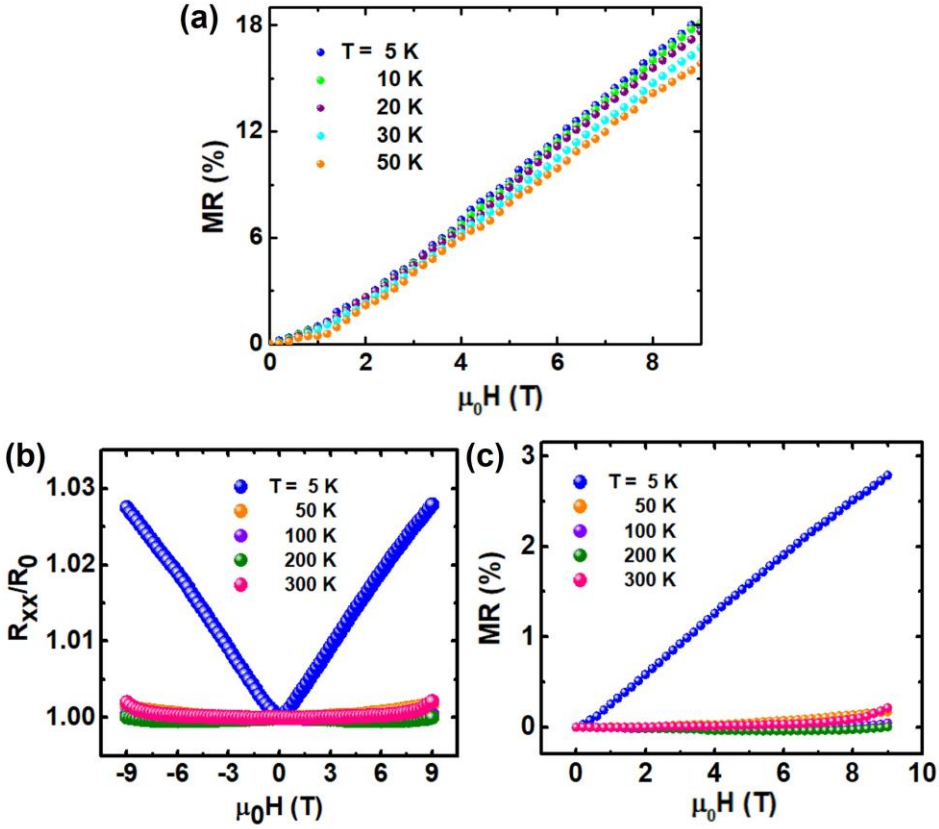

Figure S12. (a) The longitudinal MR of T_d-$Mo_{0.27}W_{0.71}Te_{2.02}$/*h*-BN as a function of magnetic field and temperature (5–50 K). Electric transport measurements of a *2H*- & T_d-$Mo_{0.22}W_{0.89}Te_{1.89}$/*h*-BN (Synthesis Route II)-fabricated device. (b) The magnetic-field dependence of the normalized longitudinal resistance (i.e., a $R_{xx}/R_0 - \mu_0 H(T)$ plot) was measured at the temperature range of 5–300 K. (c) The MR characteristics were measured at 5–300 K.

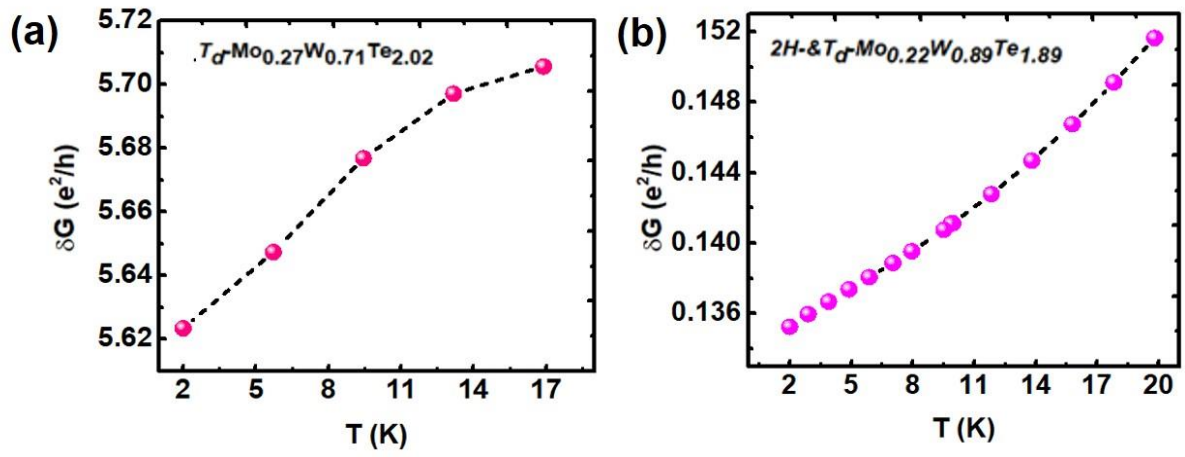

Figure S13. The temperature-dependent electrical conductance was measured for the (a) T_d-$Mo_{0.27}W_{0.71}Te_{2.02}$ /*h*-BN and (b) *2H*- & T_d-$Mo_{0.22}W_{0.89}Te_{1.89}$/*h*-BN devices.

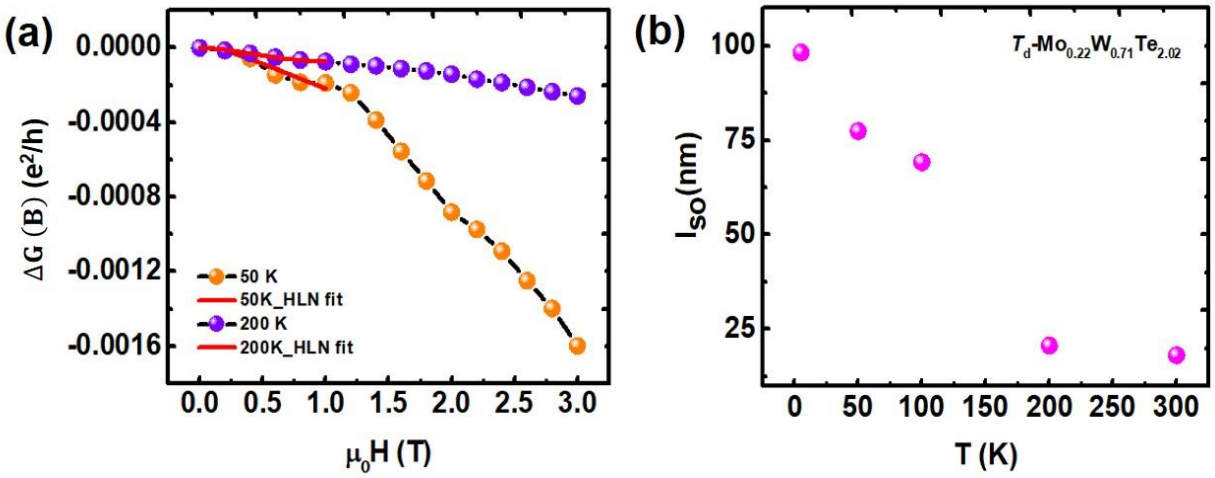

Figure S14. The magnetic field-dependent magnetoconductance (ΔG, in units of e^2/h) of a T_d-$Mo_{0.22}W_{0.89}Te_{1.89}$/*h*-BN device determined for 50 K and 200 K at the magnetic field of ≤3 T. The red solid lines indicate the corresponding HLN fits to the (ΔG) curves in the range of ≤1 T. (b) The spin-orbit interaction length (l_{so}) of T_d-$Mo_{0.22}W_{0.89}Te_{1.89}$ as a function of temperature was obtained from a least-squares fit by the HLN model.

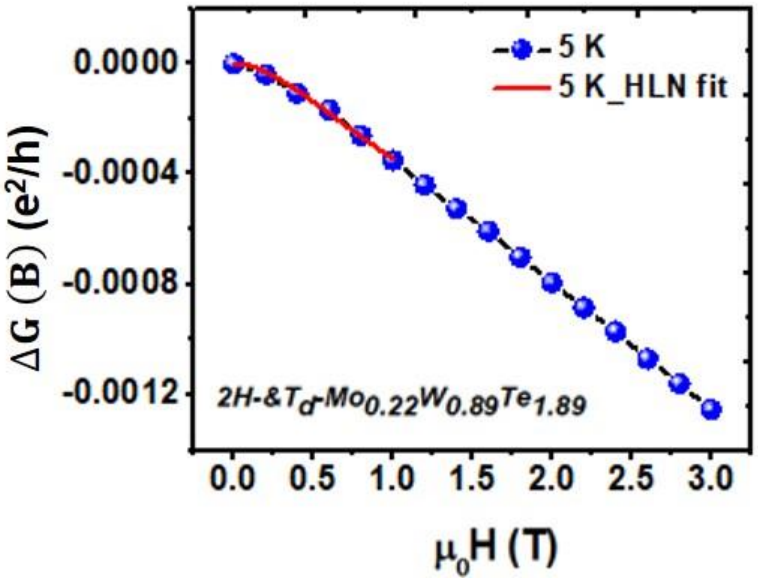

Figure S15. The magnetic field-dependent magnetoconductance (ΔG, in units of e^2/h) of a *2H*- & T_d-$Mo_{0.22}W_{0.89}Te_{1.89}$/*h*-BN device was measured at 5 K under the magnetic field of ≤3 T. The red solid line indicates the corresponding HLN fit to the (ΔG) curves in the range of ≤1 T.

References

S1. J. Zhou, F. Liu, J. Lin, X. Huang, J. Xia, B. Zhang, Q. Zeng, H. Wang, C. Zhu, L. Niu, X. Wang, W. Fu, P. Yu, T. R. Chang, C. H. Hsu, D. Wu, H. T. Jeng, Y. Huang, H. Lin, Z. Shen, C. Yang, L. Lu, K. Suenaga, W. Zhou, S. T. Pantelides, G. Liu and Z. Liu, *Adv. Mater.*, 2017, DOI: 10.1002/adma.201603471.

S2. Y. Gong, Z. Lin, G. Ye, G. Shi, S. Feng, Y. Lei, A. L. Elías, N. Perea-, R. Vajtai, H. Terrones, Z. Liu, M. Terrones and P. M. Ajayan, *ACS Nano*, 2015, **7**, 11658.

S3. J. Beck, *Synthese Und Kristallstruktur von Te42+(WC16)2 Synthesis*, 1990.

S4. M. Binnewies, R. Glaum, M. Schmidt and P. Schmidt, *Chemical Vapor Transport Reactions - A Historical Review*, Walter De Gruyter GmbH & Co. Berlin/Boston, 2013.

S5. E. Lassner and W.-D. Schubert, *Index. Tungsten Properties, Chemistry, Technology of the Element, Alloys, and Chemical Compounds Erik Lassner and Wolf-Dieter Schubert*, 1999.

S6. V. Xiv, A. Wold and J. K. Ruff, *Inorganic Synthesis*, McCraw-Hill Book Company, 1973.

S7. M. Bosi, *RSC Adv.*, 2015, **5**, 75500.

S8. A. A. Zaitsev, N. A. Korotkov and E. M. Lazarev, *Met. Sci. Heat Treat.*, 1976, **18**, 873.

S9. J. Bernède, C. Amory, L. Assmann and M. Spiesser, *Appl. Surf. Sci.*, 2003, **219**, 238.

S10. c

S11. S. M. Oliver, R. Beams, S. Krylyuk, I. Kalish, A. K. Singh, A. Bruma, F. Tavazza, J. Joshi, I. R. Stone, S. J. Stranick, A. V Davydov and P. M. Vora, *2D Mater.*, 2017, **4**, 45008.

S12. Y.-Y. Lv, L. Cao, X. Li, B.-B. Zhang, K. Wang, Bin Pang, L. Ma, D. Lin, S.-H. Yao, J. Zhou, Y. B. Chen, S.-T. Dong, W. Liu, M.-H. Lu, Y. Chen and Y.-F. Chen, *Sci. Rep.*, 2017, **7**, 44587.

S13. P. Yu, J. Lin, L. Sun, Q. L. Le, X. Yu, G. Gao, C.-H. Hsu, D. Wu, T.-R. Chang, Q. Zeng, F. Liu, Q. J. Wang, H.-T. Jeng, H. Lin, A. Trampert, Z. Shen, K. Suenaga and Z. Liu, *Adv. Mater.*, 2017, **29**, 1603991.

S14. D. Rhodes, D. A. Chenet, B. E. Janicek, C. Nyby, Y. Lin, W. Jin, D. Edelberg, E. Mannebach, N. Finney, A. Antony, T. Schiros, T. Klarr, A. Mazzoni, M. Chin, Y. C. Chiu,

W. Zheng, Q. R. Zhang, F. Ernst, J. I. Dadap, X. Tong, J. Ma, R. Lou, S. Wang, T. Qian, H. Ding, R. M. Osgood, D. W. Paley, A. M. Lindenberg, P. Y. Huang, A. N. Pasupathy, M. Dubey, J. Hone and L. Balicas, *Nano Lett.*, 2017, **17**, 1616.

S15. C. Lee, H. Yan, L. Brus, T. Heinz, J. Hone and S. Ryu, *ACS Nano*, 2010, **4**, 2695.

S16. I. H. Campbell and P. M. Fauchet, *Solid State Commun.*, 1986, **58**, 739.

S17. G. Gouadec and P. Colomban, *Prog. Cryst. Growth Charactreization Mater.*, 2007, **53**, 1.

S18. P. Parayanthal and F. H. Pollak, *Phys. Rev. Lett.*, 1984, **52**, 1822.

S19. R. Beams, L. G. Canado, S. Krylyuk, I. Kalish, B. Kalanyan, A. K. Singh, K. Choudhary, A. Bruma, P. M. Vora, F. Tavazza, A. V. Davydov and S. J. Stranick, *ACS Nano*, 2016, **10**, 9626.

S20. Y. Kim, Y. I. Jhon, J. Park, J. H. Kim, S. Lee and Y. M. Jhon, *Nanoscale*, 2016, **8**, 2309.

S21. H. Guo, T. Yang, M. Yamamoto, L. Zhou, R. Ishikawa, K. Ueno, K. Tsukagoshi, Z. Zhang, and M. S. Dresselhaus and R. Saito, *Phys. Rev. B*, 2015, **91**, 205415.

S22. M. Yamamoto, S. T. Wang, M. Ni, Y.-F. Lin, S. -L. Li, S. Aikawa, W. –B. Jian, K. Ueno, K. Wakabayashi and K. Tsukagoshi, *ACS Nano*, 2014, **8**, 3895.

S23. T. Goldstein, S.- Y. Chen, J. Tong, D. Xiao, A.Ramasubramaniam and J. Yan, *Sci. Rep.* 2016, **6**, 28024.

S24. Y.C. Jiang, J. Gao and L. Wang , *Sci. Rep.*, 2016, **6**, 19624.

S25. Y. Cao, N. Sheremetyeva, L. Liang, H. Yuan, T. Zhong, V. Meunier and M. Pan, *2D Mater.*, 2017, **4**, 035024.